Nano Energy 145 (2025) 111454

Contents lists available at ScienceDirect

Nano Energy

journal homepage: www.elsevier.com/locate/nanoen

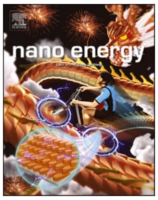

Configurational entropy-tailored borides for corrosion-resistant and durable seawater electrolysis

Shuai Chen [a], Han Zhang [a,*], Lin Wu [a], Shuo Zheng [a], Yongjia Li [a], Lixiang Li [a], Chengguo Sun [a,b], Baigang An [a,*]

[a] Key Laboratory of Energy Materials and Electrochemistry Research Liaoning Province, School of Chemical Engineering, University of Science and Technology Liaoning, Anshan 114051, China
[b] School of Chemical Engineering, Nanjing University of Science and Technology, Nanjing 210094, China

ARTICLE INFO

Keywords:
Medium-entropy boride
Photoelectrodeposition
Oxygen evolution reaction
Lattice oxygen mechanism
Electrolytic seawater

ABSTRACT

Advanced electrocatalysts that combine corrosion resistance and chloride tolerance are essential for seawater electrolysis-based hydrogen production. However, their application is limited by the lack of efficient and stable catalysts for the oxygen evolution reaction (OER). Herein, we employ an ultrafast photoelectrodeposition (PED) strategy to synthesize configurational entropy-tailored borides (MEB), which undergo in situ reconstruction into M-OOH during electrolysis, yielding an efficient and corrosion-resistant OER catalyst. Mn incorporation facilitates active sites capture of OH^- from the electrolyte, generating abundant highly active and stable oxyhydroxides. The reconstructed CoFeNiMnOOH modulates the electronic structure, activates lattice oxygen, and improves the reaction kinetics. Meanwhile, the surface effectively repels Cl^- ions, offering enhanced corrosion protection. The MEB demonstrates excellent performance in KOH-seawater electrolyte, characterized by a low overpotential (278 mV at 10 mA cm^{-2}) and outstanding long-term stability (> 4000 h). This outstanding catalytic performance positions our medium-entropy electrocatalyst among the most efficient OER catalysts reported to date for alkaline seawater electrolysis, representing a significant advancement in the development of seawater-based electrolysis technologies.

1. Introduction

Global climate change necessitates an urgent transition to sustainable energy systems. Hydrogen, as an advanced secondary energy carrier distinguished by its high heating value, cleanliness, and emission-free characteristics, plays a pivotal role in enabling international efforts toward emission reduction. The electrolysis-based hydrogen production approach emerges as a frontrunner among clean H_2 technologies, characterized by its absence of carbon discharge, ultra-pure hydrogen output, and ecologically harmless operational nature. This method effectively addresses global energy deficits while seamlessly coupling with intermittent renewable sources like solar and wind energy [1,2]. To enable large-scale sustainable hydrogen generation and efficient storage of clean renewable power, high-performance catalysts are essential. These catalysts must exhibit exceptional activity, prolonged stability, and economic viability [3–5]. However, large-scale green hydrogen production utilizing freshwater is deemed impractical due to the deficiency of freshwater resources in coastal areas and arid regions [6]. Seawater accounts for 97.3 % of water resources. Its complex composition, particularly the high concentration of Cl^-, poses substantial challenges to the stability of electrocatalysts [7]. The electrolysis of seawater mainly faces three problems: (1). The cathode surface accumulates significant quantities of cations (e.g., Ca^{2+}, Mg^{2+}) that are attracted to and adsorbed onto the cathode surface through electrostatic interactions [8]. (2) The halide ions present in seawater (e.g., Cl^-, Br^-) significantly accelerate the corrosion of electrode materials and deactivate their active sites [9]. (3). When the OER and chlorine evolution reaction (CER) reactions compete, Cl^- undergo oxidation to generate ClO^-, which substantially reduces the overall electrolytic performance [10]. These challenges render the electrocatalytic active sites ineffective and significantly impair the overall performance of the electrolytic cell. Consequently, the development of electrocatalysts that resist corrosion, suppress CER and operational stability is a critical area of research in advancing seawater electrolysis technology.

Medium and high-entropy metal systems composed of three to five metallic components have garnered considerable interest in

---

* Corresponding authors.
E-mail addresses: hzhang0807@163.com (H. Zhang), bgan@ustl.edu.cn (B. An).

https://doi.org/10.1016/j.nanoen.2025.111454
Received 21 July 2025; Received in revised form 31 August 2025; Accepted 7 September 2025

electrocatalysis [11–13]. Given their controllable compositions and the robust synergetic effects inherent in their medium-entropy architectures, demonstrate superior catalytic activity and remarkable long-term durability. Transition metal catalysts, characterized by their adjustable electronic configurations, versatile architectures, and high terrestrial abundance, offer a viable substitute for precious metals [14]. However, these catalysts experience structural degradation and material erosion under highly oxidative and corrosive conditions during prolonged OER operation, which limits their practical applicability [15]. Thus, achieving both exceptional activity and long-term stability in OER electrocatalysts still presents a critical challenge. In medium- and high-entropy borides, the electronic properties of boron atoms determine the bonding mechanisms and intrinsic bond strengths in transition metal borides [16]. These borides offer significant potential in catalysis due to the combined effects of high entropy and electron-deficient boron sites. The synthesis of entropy metal materials typically demands complex equipment and high-temperature, high-pressure conditions to ensure uniform mixing of metal elements [17].

Photoelectrodeposition (PED) has revitalized conventional electrodeposition techniques. By integrating light energy into the simple and cost-effective process of traditional electrodeposition, resulting in improved deposition rates and enhanced material quality [18]. Herein, we have successfully utilized the method of ultrafast synthesis of corrosion-resistant medium-entropy boride electrodes using photo-assisted electrodeposition technology. Upon PED, the local redox microenvironment on NF surface was modulated, thereby optimizing the electrochemical deposition dynamics. The MEB electrocatalyst demonstrates exceptional performance in seawater splitting, requiring only 278 mV overpotential to reach 10 mA cm^{-2} while exhibiting favorable kinetics (Tafel slope = 51.67 mV dec^{-1}). Notably, the catalyst maintains stable operation for over 4000 h under continuous seawater electrolysis conditions. The MEB facilitates the transformation of active sites from borides to oxyhydroxides and induces surface reconstruction, thereby enhancing catalytic performance. Moreover, the addition of Mn enhances OH^- adsorption, promotes lattice oxygen activation, and introduces electrostatic repulsion to inhibit chloride-induced corrosion, thereby improving both the corrosion resistance and catalytic activity of the catalyst in seawater environments. This work presents an innovative and effective strategy for synthesizing medium- and high-entropy electrocatalysts with enhanced performance in seawater electrolysis.

2. Experimental

2.1. Materials

All chemicals were of analytical grade and used as received. Ferrous sulfate ($FeSO_4·7H_2O$), nickel nitrate hexahydrate ($Ni(NO_3)_2·6H_2O$), cobalt nitrate hexahydrate ($Co(NO_3)_2·6H_2O$), manganese sulfate ($MnSO_4·H_2O$), potassium borate ($K_2B_4O_7·4H_2O$), potassium hydroxide (KOH), ruthenium oxide (RuO_2), and ethanol were procured from Sinopharm Chemical Reagent Co., Ltd.

2.2. Synthesis of MEB

Nickel foam (3 cm × 4 cm) was ultrasonically cleaned in ethanol for 30 min, then immersed in 1 M HNO_3 for 1 h to remove the surface oxide layer. It was subsequently rinsed three times with deionized water and dried under vacuum at 60 °C for 12 h. The preparation of MEB began by dissolving stoichiometric amounts of metal salts, 0.16 mmol $FeSO_4·7H_2O$, 0.08 mmol $Co(NO_3)_2·6H_2O$, 0.08 mmol $Ni(NO_3)_2·6H_2O$, 0.08 mmol $MnSO_4·H_2O$, and 0.25 mol $K_2B_4O_7·4H_2O$ in 200 mL of DI water, which as a proton receptor (pH 7–9 buffer system). The resulting solution was homogenized via ultrasonication for 30 min. The medium-entropy boride (MEB) was photoelectrodeposition onto pretreated nickel foam (working electrode) using a standard three-electrode configuration with Pt and Ag/AgCl as counter and reference electrodes, respectively. Under AM 1.5 G simulated sunlight, a constant potential of −0.30 V (vs. Ag/AgCl) was maintained for 1 min. Following the deposition process, the electrode was carefully rinsed with DI water to eliminate residual ions before OER testing. The final product was labeled as MEB.

3. Results and discussion

3.1. Synthesis and characterization

The detailed synthetic process of MEB using one-step ultrafast photoelectrodeposition (PED) method is illustrated in Fig. 1a. Firstly, pretreated nickel foam was cut into 1 × 1 cm pieces and subjected to PED for only 1 min at a constant potential of −0.3 V (vs. Ag/AgCl). Potassium tetraborate solution served a dual role as both a pH buffer (maintaining pH 7–9) and a boron source for MEB catalyst formation. As observed by scanning electron microscopy (SEM), the MEB displayed a roughened surface with a uniform distribution of B, O, Co, Fe, Mn, and Ni elements. Moreover, the aggregated MEB nanoparticles formed a dense thin-film structure (Fig. S1) [19]. The structural advantages of MEB arise from the introduction of boride groups and increased surface roughness, which collectively reduce the contact angle from 101.6° (NF) to 21.1° (MEB) (Fig. S2) [20]. Compared to the conventional electrodeposition method, the PED method yields smaller nuclei with uniform dispersion, demonstrating that photo-assisted deposition promotes the homogeneous co-deposition of Fe, Co, Ni, and Mn (Fig. S3). Simultaneously, X-ray photoelectron spectroscopy (XPS) analysis revealed decreased peak intensities for B, Co, Mn, and Fe, but an enhanced Ni signal in the PED samples compared to those obtained by electrodeposition, which can be attributed to reduced deposition rates limiting substrate coverage (Fig. S4). Transmission electron microscopy (TEM) analysis of ultrasonically exfoliated MEB catalysts revealed lattice fringes with a spacing of 0.206 nm, corresponding to the (110) plane of CoFeB [21]. Elemental mapping showed a uniform spatial distribution of all five elements (B, Co, Fe, Ni, Mn), confirming successful incorporation without phase segregation (Fig. 1b-e). In addition, Fourier-transform infrared (FT-IR) spectroscopy identified characteristic vibrational modes that unambiguously confirm the formation of M-(BO_3) species in MEB (Fig. 1f). FT-IR analysis of MEH revealed the absence of characteristic BO_3 and M-O-B absorption peaks. Instead, distinct vibrational modes corresponding to OOH, O-O, and M-OH groups were identified, confirming the leaching of boron from the material structure (Fig. S5). X-Ray Diffraction (XRD) patterns reveal three distinct peaks at 44.48°, 51.83°, and 76.35° (Fig. S6), corresponding to the (111), (020), and (022) planes of fcc nickel (PDF#04–0850). Simultaneously, MEB powder exhibits two broad peaks that align with the weak peaks of FeB, demonstrating its amorphous and low-crystallinity characteristics (Fig. S7) [22–25]. Secondly, cyclic voltammetry (CV) activation transformed the morphology of MEB from a thin-film structure into two-dimensional nanoarrays, forming medium-entropy oxyhydroxides (MEH) (Fig. S8). High-resolution transmission electron microscopy (HR-TEM) revealed well-defined nanosheets with lattice spacings of 0.200 nm and 0.244 nm, corresponding to the (018) and (104) planes of NiOOH, respectively. Raman spectroscopy confirmed the irreversible phase transformation, as evidenced by the emergence of M-OOH peaks in MEH (Fig. S9). These structural changes facilitate more efficient interactions between reactants and active sites, thereby enhancing the catalytic performance [26].

Ultraviolet photoelectron spectroscopy (UPS) was used to quantify the charge transfer effect [27,28]. As shown in Fig. S10, Mn incorporation in MEB modifies the electronic band structure, raising the valence band maximum (E_{VB}) from 3.78 eV in CoFeNiB to 4.80 eV. This higher E_{VB} reduces the energy required for interaction with adsorbates. Additionally, the low kinetic energy cutoff (E_{cutoff}) of MEB increased by 0.68 eV, corresponding to a decrease in the work function from 4.12 eV to 3.44 eV due to Mn. These modifications facilitate electron transfer

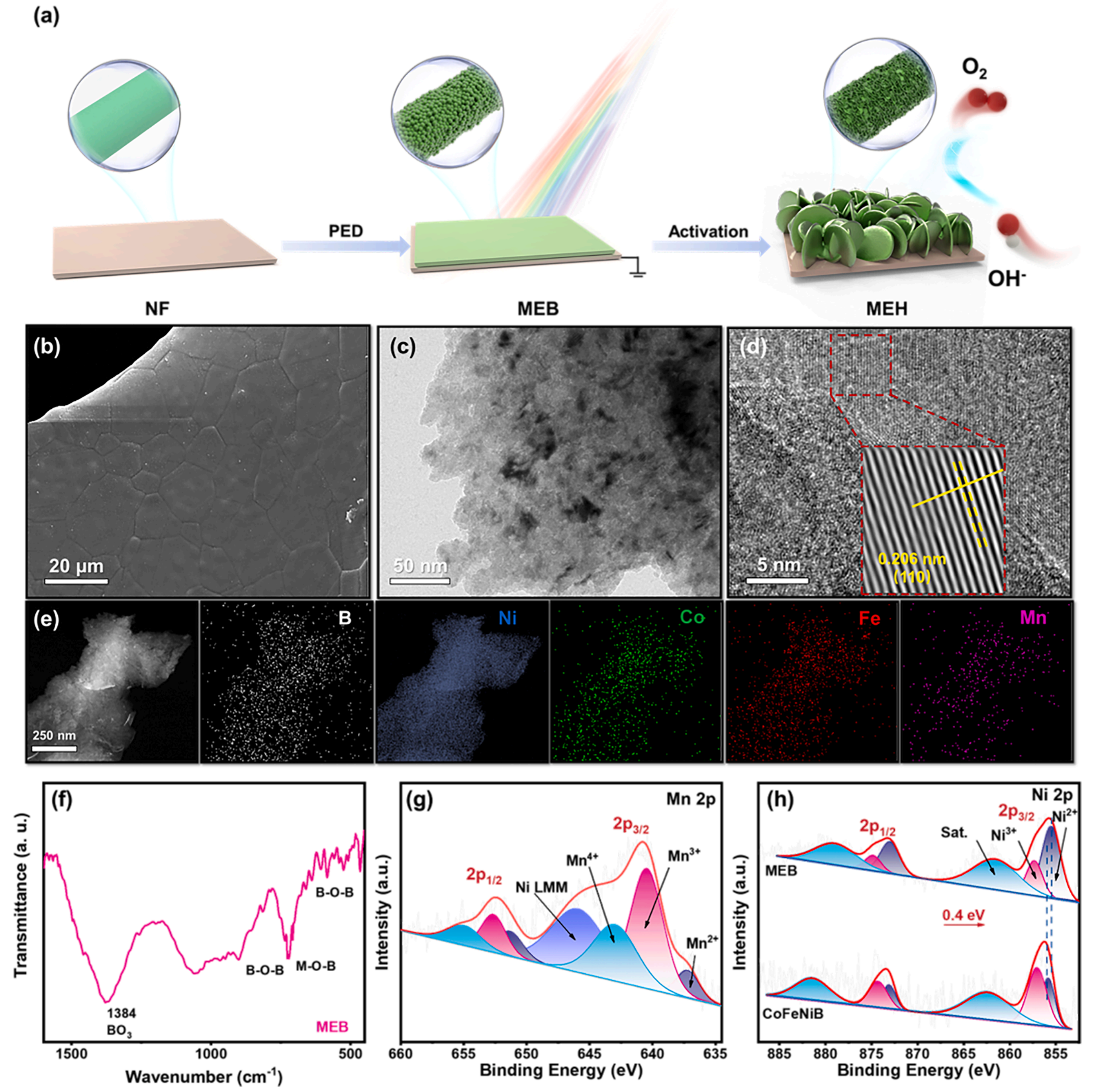

Fig. 1. (a) MEB structures of different structural systems were prepared using a one-step photoelectrodeposition technique. (b) The SEM images of MEB. (c) The HR-TEM image of MEB. (d) The lattice fringe images of MEB. (e) The element distribution mapping of TEM-EDS. (f) The FT-IR spectroscopy of MEB. The XPS of (g) Mn and (h) Ni.

from the bulk to the surface, enhancing electrocatalytic performance. XPS was employed to investigate the elemental distribution and oxidation states of CoFeNiB and MEB. As shown in Fig. 1g, the Mn 2p spectrum displays four well-defined peaks at 637.3 eV (Mn^{2+}), 640.9 eV (Mn^{3+}), 643.7 eV (Mn^{4+}), and 646.9 eV (Ni LMM), indicating the coexistence of multiple oxidation states. Such mixed-valence states, which are typical for transition-metal-based catalysts, promote surface reconstruction and thereby enhance catalytic performance [29,30]. The Co, Fe, and Ni 2p spectra display characteristic doublets in the $2p_{3/2}$ and $2p_{1/2}$ regions, confirming the presence of both +2 and +3 oxidation states. Notably, the incorporation of Mn alters the electronic environment of Ni, Fe, and Co, as evidenced by a 0.30–0.40 eV shift of the MEB peaks toward lower binding energies. This shift promotes electron transfer to the metal centers, thereby potentially enhancing the catalytic efficiency of the active sites (Fig. S11 and Fig. 1h) [30]. The MEB catalyst successfully incorporates boron as borate anions, as evidenced by the B 1 s XPS peak at 191.9 eV (Fig. S11d), corresponding to the B^{3+} oxidation state in borate-like M-(BO_3) structures [31].

3.2. *OER performance*

The OER performance of the catalysts was assessed in a 1 M KOH solution using a standard three-electrode setup. Linear Sweep Voltammetry (LSV) measurements revealed that the MEB catalyst achieved a current density of 10 mA cm^{-2} at a low overpotential of 248 mV, demonstrating enhanced electrocatalytic activity. This overpotential of the catalyst is significantly lower than that of various materials, including commercial RuO_2 (275 mV), CoFeMnB (302 mV), FeNiMnB (311 mV), CoNiMnB (328 mV), CoFeNiB (313 mV) and pure NF (399 mV) (Fig. 2a and Fig. S13). MEB demonstrates outstanding catalytic efficiency under industrial-scale operating conditions, maintaining an overpotential of 350 mV at 400 mA cm^{-2}, demonstrating its outstanding catalytic efficiency and exceptional suitability for large-scale water splitting systems. Moreover, MEB demonstrates outstanding electrocatalytic performance for the OER, with a remarkably low Tafel slope (33.42 mV dec^{-1}) that outperforms commercial RuO_2 (50.27 mV dec^{-1}) and CoFeNiB (52.42 mV dec^{-1}) by significant margins (Fig. 2b and 2c). With a Tafel value of 33.42 mV dec^{-1}, the catalytic mechanism appears to be dominated by the formation of *OOH/OO intermediates during the rate-determining step (RDS), indicative of a single-electron transfer preceding the oxygen-oxygen coupling event [32–34]. To investigate the charge-transfer dynamics, electrochemical impedance spectroscopy (EIS) was performed. The Nyquist plots depicted in Fig. S12 were fitted utilizing a hypothetical equivalent circuit model, which is constituted of three distinct components [35]. The Nyquist plots revealed that MEB exhibits the lowest charge-transfer resistance (0.47 Ω), significantly lower than that of RuO_2 (1.17 Ω) and CoFeNiB (1.74 Ω) (Fig. 2d and Table S1). The low resistance at the electrode-electrolyte interface facilitates efficient electron transfer, which is crucial for high catalytic performance [36]. It is noteworthy that MEB manifests the smallest values for both R_2 and R_1, thereby signifying its heightened tendency towards oxidation and reconstruction processes. This performance not only surpasses that of benchmark catalysts, but also indicates the presence of optimized reaction pathways with reduced energy barriers for intermediate formation.

The electrochemical active surface area (ECSA) of electrocatalysts exhibits a linear correlation with their double-layer capacitance (C_{dl}), as established in prior studies [37]. CV scans across a 10–50 mV s^{-1} range in the non-Faradaic potential window revealed a linear correlation between capacitive current and scan rate, enabling precise ECSA quantification and characterization of the electrode's capacitive behavior. Subsequent analysis revealed distinct C_{dl} values, with MEB exhibiting a significantly higher capacitance (144.1 mF cm^{-2}) compared to CoFeNiB (106.9 mF cm^{-2}) (Fig. 2e and Fig. S14) [38]. To isolate intrinsic catalytic activity from surface-area effects, we evaluated both turnover frequency (TOF) and ECSA-normalized current density. The MEB's reaction rate of up to 2.938 s^{-1} at 1.55 V vs. RHE compared to other materials (FeNiMnB: 0.122 s^{-1}, CoFeNiB: 0.774 s^{-1}, CoNiMnB: 0.170 s^{-1}, CoFeMnB: 0.144 s^{-1} and NF: 0.011 s^{-1}) (Fig. S15 and Table S2). Notably, MEB exhibits a TOF value of 1.64 s^{-1} at η_{300}, outperforming CoFeNiB (0.296 s^{-1}) by more than fivefold, which highlights its markedly improved OER efficiency (Fig. 2f). Consequently, the incorporation of Mn activates additional catalytic sites and enhances the intrinsic catalytic activity, enabling MEB to deliver superior performance. The results indicate that MEB exhibited the best catalytic performance

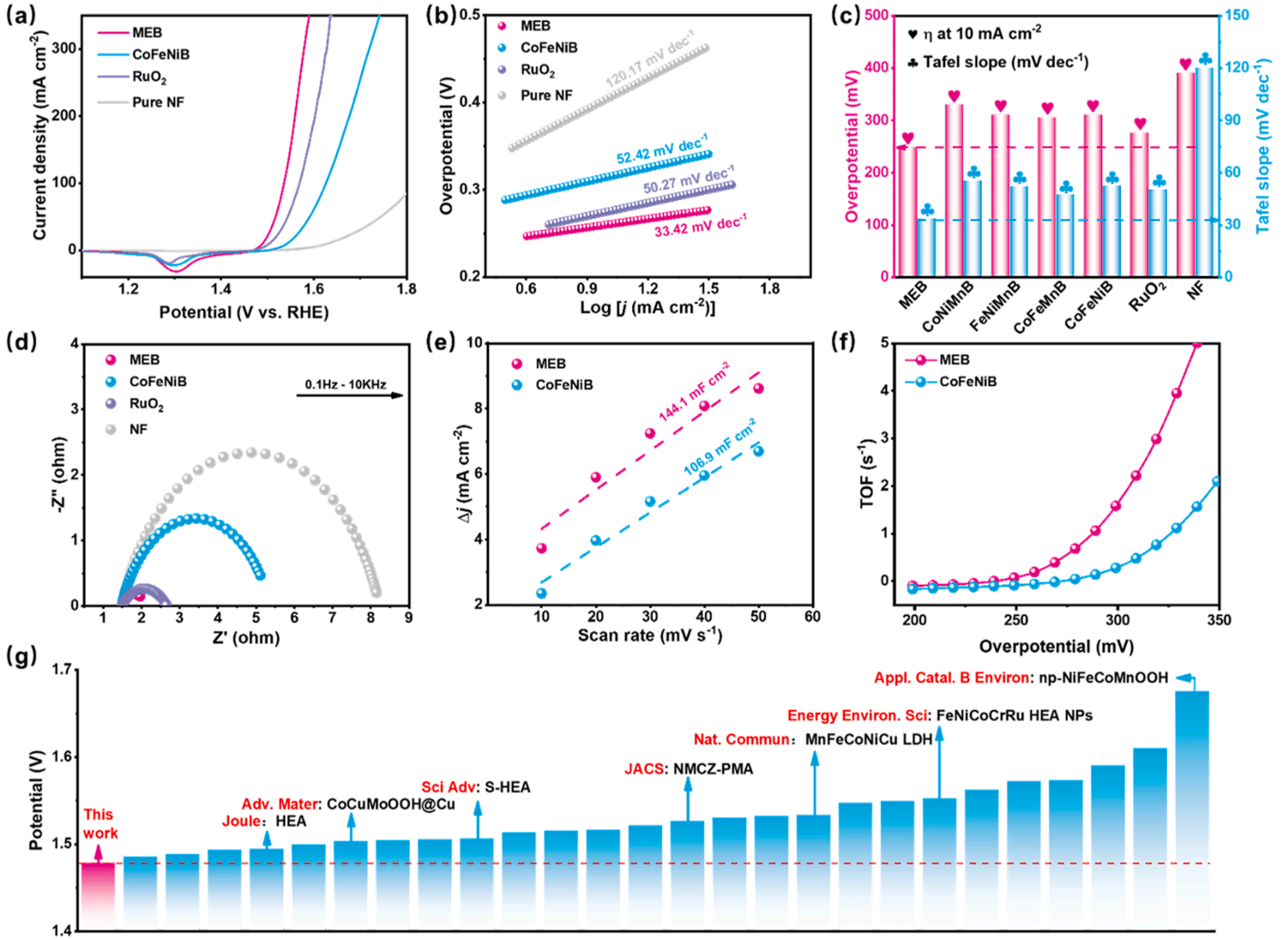

Fig. 2. (a) OER LSV curves of MEB, CoFeNiB, commercial RuO_2, and pure NF. (b) Tafel plots. (c) The bar graph of overpotentials and Tafel slope. (d) Nyquist plots at 1.51 V. (e) C_{dl} plots. (f) TOFs plots. (g) Comparison diagram of activity with other reported catalysts.

among comparative samples, with significantly superior normalized OER activity compared to CoFeNiB (Fig. S16). The OER selectivity of MEB in alkaline electrolyte was evaluated by determining its Faradaic efficiency (FE) via the drainage method and gas collection analysis. An H-type electrolysis cell was employed to monitor gas production at 200 mA cm^{-2} over 550 s. The measured volumes of H_2 (12.6 mL) and O_2 (6.3 mL) exhibited the expected 2:1 stoichiometric ratio, consistent with water splitting (Fig. S17 and S18). This resulted in a consistent volume ratio of $V_{H2}/V_{O2} = 2:1$ throughout the reaction process. The measured volumes closely matched the theoretical values derived from relevant equations. These results indicate that the FE for electrocatalytic overall water splitting in alkaline electrolyte is approaching 100 %.

The durability of OER catalysts is a key determinant of their practical viability, requiring consistent performance over time. Remarkably, LSV analysis demonstrated that MEB maintained its catalytic activity after 1000 CV cycles, with even a slight but measurable performance increase (Fig. S19a). This enhancement is attributed to the dynamic surface restructuring of the catalyst during cyclic voltammetry, wherein the MEB pre-catalyst is in situ transformed into MEH [39,40]. The catalytically active MEB demonstrates stable operation across a range of potentials (1.5 V−1.9 V) (Fig. S19b). Chronopotentiometric testing showed that the catalyst maintained consistent performance over 400 h at 100 mA cm^{-2}, with a remarkably slow potential degradation rate of only 0.04 μV h^{-1} (Fig. S20). Because industrial electrolysis requires catalysts to withstand harsh conditions over extended periods, an AEMWE system was constructed using MEB as the anode and Raney nickel mesh as the cathode. The system demonstrated stable performance at 2.0 V and 1 A cm^{-2} over 160 h of continuous operation, further exceptional MEB's suitability for practical applications (Fig. S21). Moreover, the MEB electrode outperforms most reported catalysts in catalytic efficiency (Fig. 2g and Table S3), making it a highly promising candidate for sustainable electrolysis applications.

To systematically investigate the roles of light, electrical potential, and deposition dynamics in the synthesis process, we conducted a comprehensive study. MEB exhibited significantly enhanced material properties compared to samples prepared without the photo-assisted method. The results demonstrate that under photo-assisted condition, the OER performance of MEB is enhanced by 137 mV, as evidenced by polarization curves showing a significant improvement. Moreover, the electrical resistance of MEB is notably reduced compared to that of samples synthesized without light exposure. Furthermore, as shown in Fig. S22 and S23, the ECSA of MEB increases by 38 % under PED compared to dark conditions. Collectively, these results confirm that photo-assisted electrodeposition effectively enhances both the structural and electrochemical performance of MEB. Subsequently, the effect of varying PED durations was systematically investigated. The sample subjected to 1-minute PED exhibits superior OER activity, optimal polarization behavior, and the lowest impedance compared with the 30-second and 1-hour samples. SEM analysis further reveals that illumination duration strongly influences MEB deposition (Fig. S24). Furthermore, both excessively short and prolonged PED times result in reduced ECSA values relative to the 1-minute condition (Fig. S25). PED is driven by light-enhanced nucleation and growth of the catalyst. The applied potential controls the mass loading, with an optimal bias maximizing deposition efficiency. Prolonged deposition can cause nanoparticle aggregation, reducing active site accessibility and performance (Fig. S26). As a result, the deposition reaction kinetics are significantly improved.

Seawater electrolysis offers a sustainable approach due to the vast abundance of seawater. However, the presence of Cl^- ions and severe corrosion during electrolysis can suppress the OER and lead to gradual electrode degradation [9,10]. Seawater collected from the Yellow Sea (Dalian, China) underwent systematic purification prior to experimental use (Fig. S27 and S28). To evaluate the industrial potential of the MEB catalyst, its performance was evaluated in 1 M KOH + 0.5 M NaCl and 1 M KOH + seawater [41]. The MEB catalyst exhibited overpotentials of 252 mV in simulated seawater and 278 mV in alkaline seawater electrolytes to achieve a current density of 10 mA cm^{-2} (Fig. 3a), and Tafel slopes of 38.69 mV dec^{-1} and 51.67 mV dec^{-1} in simulated and alkaline seawater, respectively (Fig. 3b). To demonstrate superior electrochemical stability in alkaline seawater, as demonstrated by the Tafel corrosion polarization curves of MEB, CoFeNiB, and NF were analyzed under alkaline conditions and compared (Fig. S29) [42,43]. The MEB exhibits the lowest corrosion current density (5.94 μA cm^{-2}) and highest potential (1.18 V vs. RHE), outperforming CoFeNiB (12.65 μA cm^{-2}, 1.05 V) and pure NF (24.23 μA cm^{-2}, 0.73 V), confirming its superior stability (Fig. 3c). Meanwhile, the Tafel curves and impedance of MEB and CoFeNiB in different electrolytes were investigated. MEB maintains a higher corrosion potential (1.02 V), a lower corrosion current density (19.19 μA cm^{-2}), and lower impedance (5.50 Ω) in seawater electrolytes (Fig. S30) compared to CoFeNiB (0.92 V, 70.22 μA cm^{-2} and 7.1 Ω). The higher corrosion potential of MEB indicates enhanced corrosion resistance, while the lower corrosion current density reflects a reduced corrosion rate. These results indicate that the introduction of Mn enhances its corrosion resistance and charge transfer resistance under alkaline seawater conditions.

The hypochlorite detection method using N, N-diethyl-p-phenylenediamine (DPD) as a colorimetric indicator is illustrated in Fig. 3d, with quantitative analysis performed post-stability testing via UV-Vis spectroscopy [44,45]. During the durability assessment, optical imaging was utilized to monitor real-time changes in ClO^- concentration within the electrolyte. The electrolyte from the MEB catalyst remained colorless and transparent throughout the testing period, whereas the CoFeNiB electrolyte exhibited noticeable discoloration by 100 h. Remarkably, MEB maintains an extremely low signal after 3000 h, as confirmed by UV-Vis spectroscopy, demonstrating its outstanding stability and chlorine evolution reaction (CER) selectivity (Fig. 3e). Extended testing up to 3000 h reinforces this superior CER selectivity. Moreover, the selectivity between CER and OER was found to be pH-dependent. Therefore, selectivity assessments were conducted in alkaline seawater under various pH conditions. Operating at pH 14 effectively suppresses the CER and ensures selective OER (Fig. S31) [46]. After 1100 s of electrolysis, 12.4 mL of H_2 and 24.8 mL of O_2 were produced, corresponding to a Faradaic efficiency of 97.18 % (Fig. S32). These results confirm that the primary reaction is OER rather than CER, thereby validating the excellent OER selectivity of the MEB catalyst. Furthermore, the MEB catalyst exhibits a significant 110 mV reduction in OER overpotential in 6 M KOH + seawater, compared to alkaline seawater (Fig. 3f and Fig. S33). Moreover, after 4000 h of testing, compared with most reported catalysts, no obvious changes in activity were observed (Fig. 3g and Table S4). In contrast, CoFeNiB and NiB exhibited noticeable performance degradation after only 200 h of testing (Fig. S34). Under harsh conditions and high current densities, the catalyst maintains remarkable stability, indicating its promising prospects for industrial-scale seawater electrolysis.

3.3. *Insight into OER mechanism and Cl^- repulsion*

To understand why the MEB show better OER activity, we studied the reaction kinetics. We calculated the activation energy using LSV polarization curves. The measurements were taken at different temperatures (300 K to 320 K) [47]. In general, reactants need to possess kinetic energy higher than the energy barrier to form products. When temperature rises, the molecules move faster. This gives them more energy to overcome the reaction barrier. As a result, the OER requires less extra voltage to proceed [48]. When the reaction temperature increases from 300 K to 320 K, more reactants participate in the reaction (Figs. 4a and 4b). Consequently, the OER overpotentials of the MEB and CoFeNiB samples are significantly reduced. Additionally, the data demonstrate that at 328 mV, the activation energy (E_a) of MEB is 29.10 kJ mol^{-1}, while that of CoFeNiB is 51.51 kJ mol^{-1}. The data shows that higher temperatures lower the overpotential for both

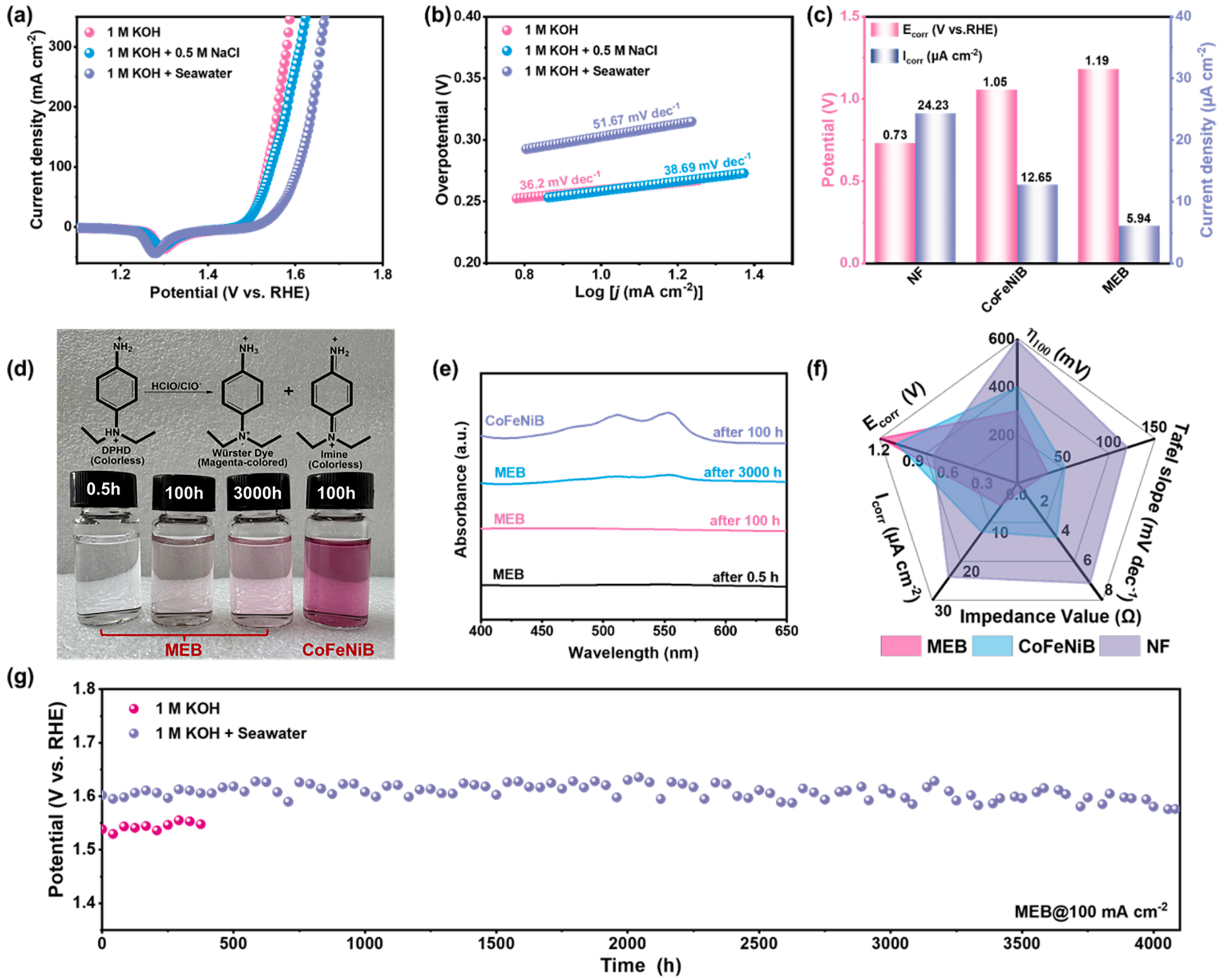

Fig. 3. (a) Polarization curves obtained in alkaline electrolyte, simulated seawater and alkaline seawater. (b) Tafel plots. (c) Corrosion bar chart. (d) The DPD mechanism and optical image after stability test. (e) The UV–vis absorption profile of the alkaline seawater following the stability test. (f) Comparisons of overpotential, Tafel slope, Impedance value, Corrosion current and Corrosion voltage. (g) Long-term stability test of MEB.

catalysts. For the MEB, the overpotential drops from 247 mV to 231 mV, and similarly, CoFeNiB's overpotential decreases from 307 mV to 276 mV (Fig. 4a and 4b), with the apparent E_a derived from the slope of the Arrhenius plot. Furthermore, the E_a of the two catalysts under different overpotentials were calculated based on the Arrhenius equation (Fig. S35). It can be observed that the E_a of MEB is lower than that of CoFeNiB under all overpotentials (Fig. S35d and Table S5). These results show that MEB has a much lower energy barrier than CoFeNiB during the OER process, with the incorporation of Mn substantially lowering the activation energy barrier for oxygen evolution and thereby facilitating the reaction kinetics.

To explore interfacial characteristics at the electrode-electrolyte interface and elucidate reactant adsorption behavior, we employed in situ EIS testing coupled with Laviron equation analysis for quantitative evaluation of *OH adsorption on catalytic surfaces [32,49,50]. Measured from Nyquist plots (Fig. S36), the total resistance of MEB and CoFeNiB reveals that Mn incorporation in MEB lowers its charge transfer resistance, enhancing interfacial charge transfer kinetics and surface activity. This improvement reflects Mn's role in facilitating electron exchange at the catalyst-electrolyte interface, while changes in overall resistance can serve as an indicator of OH adsorption behavior-a key parameter in catalytic performance. MEB has a resistance of 80 Ω, much lower than CoFeNiB (400 Ω) at 1.3 V. This means MEB adsorbs *OH faster with less driving potential. The Bode plot reveals how the electrocatalyst's performance and the OER process evolve over time, and how the phase angle shifts with frequency (Fig. 4c and 4d). Typically, the phase angle peak at low frequencies is tied to the catalyst's surface charge transfer and inner-layer electron transfer, while the peak at high frequencies is linked to the OER process and the electrocatalyst's electro-oxidation activity. With the potential at 1.25 V, the phase angle of MEB reduces more rapidly in the high-frequency segment, highlighting significant electro-oxidation activity of the electrocatalyst and quick inner-layer charge transfer. In contrast, CoFeNiB exhibits intense reactions solely at a potential of 1.4 V. In the low-frequency segment, the smaller phase angle indicates substantial OER activity for MEB after 1.3 V (Fig. 4c), whereas CoFeNiB exhibits similar activity starting at 1.4 V (Fig. 4d). The MEB exhibits superior electrochemical performance relative to CoFeNiB, as evidenced by improved *OH adsorption kinetics and charge transfer efficiency. To further elucidate the underlying mechanisms, the behavior of adsorbed *OH species on the electrocatalyst was investigated using the Laviron equation. The steady-state REDOX currents were linearly related to the square root of the potential scanning rate (Fig. S37) [51,52]. As shown in Fig. 4e and 4f, the K_s values of MEB is 0.163 s^{-1}, which is larger than that of CoFeNiB

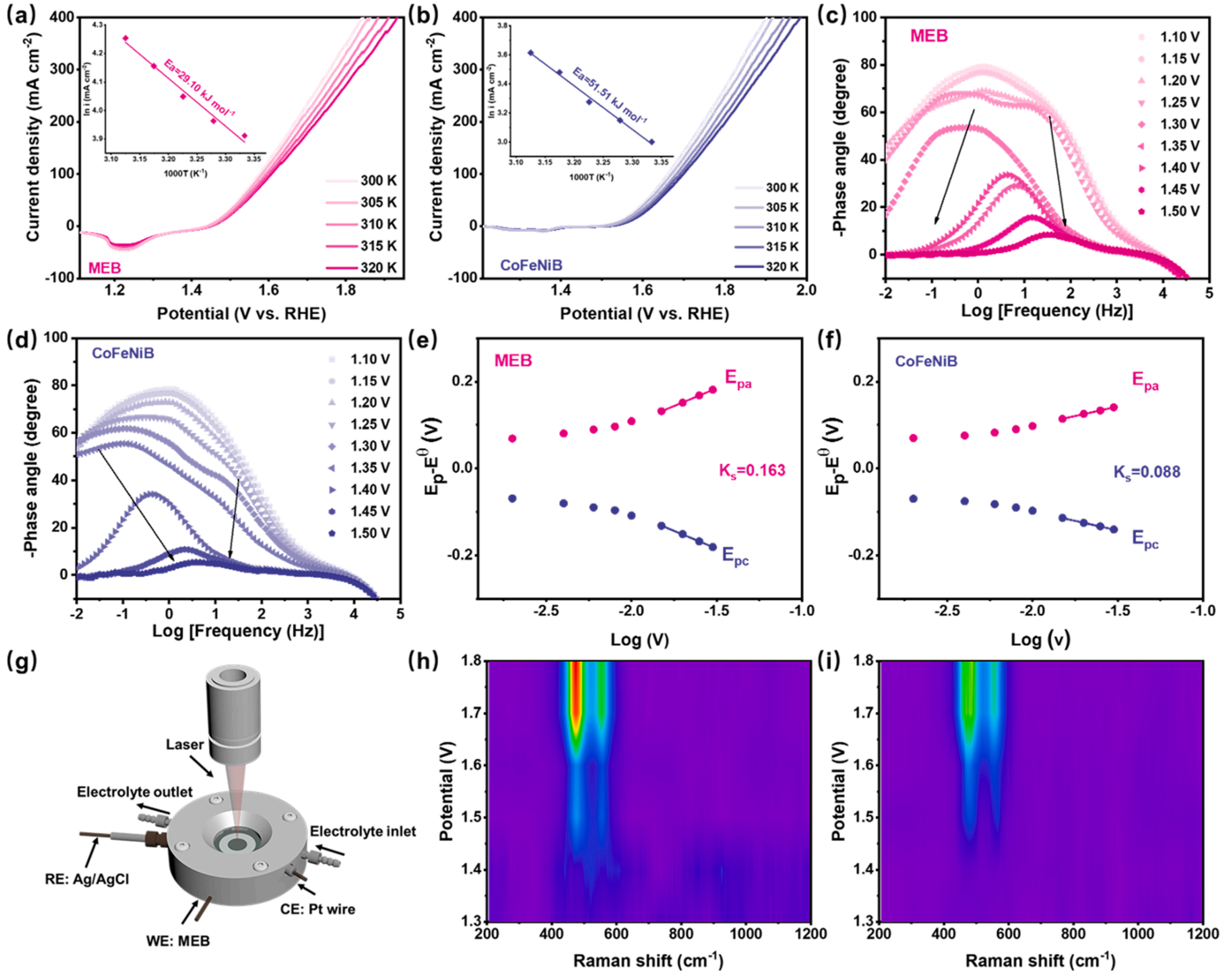

Fig. 4. (a) OER polarization curves of MEB and (b) CoFeNiB measured at sweep rates of 5 mV s^{-1} at different temperatures (300 K- 320 K). Bode plots for (c) MEB and (d) CoFeNiB at range of 1.1–1.5 V. The plot of the redox peak potentials versus the logarithm of scan rate of (e) MEB and (f) CoFeNiB. (g) A schematic representation of the operando Raman experimental setup. Operando Raman spectroscopy of (h) MEB and (i) CoFeNiB at various potentials.

(0.088 s^{-1}). The incorporation of Mn into MEB significantly improves its electrochemical performance, evidenced by reduced resistance, enhanced *OH adsorption kinetics, and superior catalytic activity relative to CoFeNiB. In summary, MEB demonstrates faster charge transfer on the surface and within the inner layer, showcasing superior electrochemical performance compared to CoFeNiB. This performance enhancement stems from synergistic electronic coupling effects that simultaneously optimize adsorption thermodynamics and accelerate kinetic processes.

To in-depth research deeper into the structure of the catalyst after activation, high-resolution XPS was utilized. Compared with MEB before activation, the MEH exhibited increased ratios of Fe^{3+}/Fe^{2+} (1.155), Co^{3+}/Co^{2+} (1.143), Ni^{3+}/Ni^{2+} (0.755), and $Mn^{3+/4+}/Mn^{2+}$ (17.911) (Fig. S38a-d). Simultaneously, the near-disappearance of B elemental peaks in the XPS spectrum after cycling confirms a significant reduction in surface B content, likely resulting from boron dissolution into the electrolyte during the reaction (Fig. S38f and Table. S6). The high-resolution XPS spectrum of the MEB catalyst after testing shows M-O makes up 22.05 % of the surface. This suggests the catalyst slowly oxidizes to form M-OOH, which is likely the key active species driving the OER (Fig. S38e and Table S7). Electron-deficient boron acts as an electron trap by accepting delocalized electrons from the metal, thereby facilitating the formation of active species through the M(II)-OH → M (III)-OOH transformation. This electron-trapping effect optimizes the electronic structure of the metal centers, while Mn facilitates electron transfer to the metal, potentially enhancing the catalytic efficiency of the active sites [53].

This structural change is driven by electrochemical reactions during operation. HR-TEM and EDS mapping (Fig. S8) characterize the MEH structure and confirm the presence of M-OOH as the active site for the OER in MEB. To elucidate the realistic active sites for OER on the MEB catalyst, operando Raman measurements were performed under realistic electrolysis conditions. The electrochemical cell used a standard three-electrode setup: MEB (WE), Pt wire (CE), and Ag/AgCl (RE) (Fig. 4g). The electrolyte (1 M KOH) flows over the surface of MEB to remove the gas bubbles generated during the reaction. A focused laser was directed through a quartz viewing port, irradiating the MEB surface to track dynamic variations in reactive intermediates throughout the OER. The thermodynamic spectra of in situ Raman revealed that both MEB and CoFeNiB maintained structural stability below 1.30 V (Fig. 4h and 4i). Upon increasing the applied potential, MEB exhibited prominent vibration peaks at 475 cm^{-1} and 553 cm^{-1}, corresponding to the E_g (Ni-O bending) and A_{1g} (Ni-O stretching) vibrational modes of (CoFe) NiOOH, respectively [25,54–56]. The applied potential reaching 1.8 V led to changes in the Raman peak intensity ratio (I_{475}/I_{553}), confirming the formation of (CoFe)NiOOH on the MEB surface. The increasing concentration of (CoFe)NiOOH indicated continuous catalyst reconstruction. Notably, MEB initiated the formation of (CoFe)NiOOH species at a relatively low potential of 1.4 V, whereas CoFeNiB required higher potentials to trigger surface restructuring. In-situ Raman spectroscopy revealed that (CoFe)NiOOH phases form at higher potentials and are largely retained upon returning to OCP (Fig. S39). The peak evolution indicates that the surface reconstruction is predominantly irreversible. Mn incorporation accelerates stabilization of these M-OOH phases, facilitating a mechanistic shift from the AEM to LOM pathway. Additionally, after 800 s of stability testing, weak FeOOH signals were observed, presumably due to Fe dissolution and subsequent redeposition during the OER process (Fig. S40). ICP-MS analysis (Table S6) indicated a notable increase in Fe concentration in the electrolyte after 2 h, followed by a considerable decrease over the subsequent 12 h durability test, implying the redeposition of FeOOH [57].

To experimentally validate the mechanism, we conducted pH-dependent tests and employed tetramethylammonium (TMA^+) ions as molecular probes to investigate the oxygen transfer pathways [57,58]. Given that lattice oxygen mechanism (LOM) proceeds via a non-concerted proton-electron transfer process and exhibits pronounced pH-dependent behavior [59], we investigated the pH sensitivity of MEB and CoFeNiB (Fig. 5a). The OER performance of MEB displayed strong pH dependence, with a slope of 93 mV pH^{-1}, whereas CoFeNiB exhibited only marginal sensitivity (53 mV pH^{-1}), further supporting the dominance of LOM in Mn-modified catalysts. The lattice oxygen-mediated mechanism facilitates O-O bond formation through a direct coupling pathway, creating active surface sites on the adsorbate evolution mechanism (AEM) that stabilize transient superoxide (O_2^-) and peroxide (O_2^{2-}) intermediates [60]. This observation suggests TMA^+ cations serve as effective molecular probes for detecting anionic oxygen intermediates through selective electrostatic interactions. The diagnostic capability is evidenced by MEB's OER performance showing dramatic deterioration upon TMA^+ introduction, whereas CoFeNiB maintained stable catalytic activity under identical conditions (Fig. 5b). The experimental data reveal that manganese incorporation markedly enhances the generation of oxygenated intermediates during OER, confirming the activation of the LOM pathway [61]. Collectively, both the TMA^+ probe assay and pH-dependent activity trends provide conclusive evidence for LOM activation in MEB. Additionally, Raman spectroscopy revealed distinctive peaks at 750 cm^{-1} and 947 cm^{-1} in the MEB sample under TMA^+ conditions, neither of which were detected in CoFeNiB (Fig. 5c). The characteristic peak of O_2^{2-} species was exclusively observed in MEB, confirming that MEB follows the LOM pathway [62].

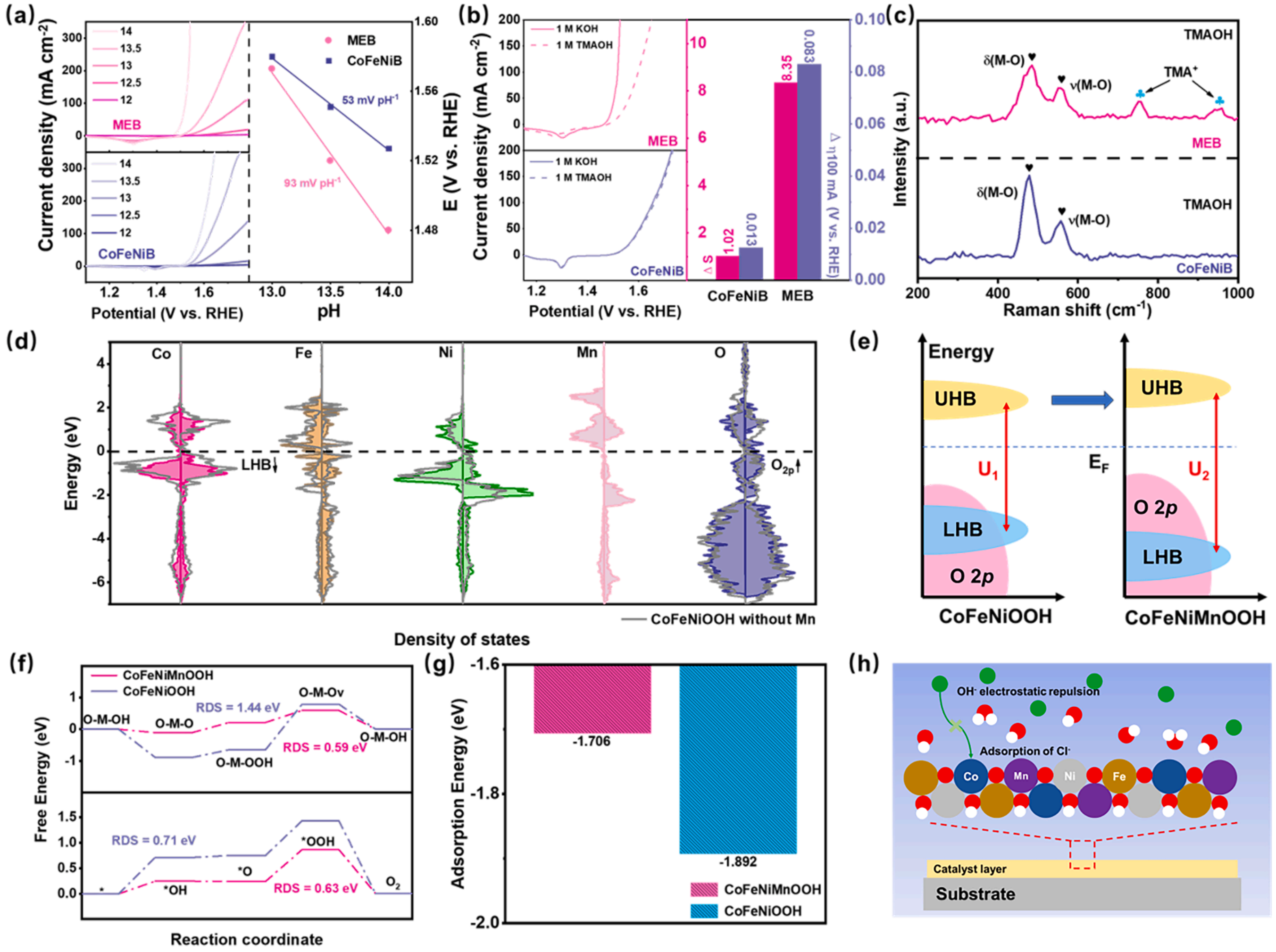

Fig. 5. (a) The logarithmic current density of MEB and CoFeNiB at 100 mA cm^{-2} was evaluated as a function of pH. (b) LSV curve of MEB and CoFeNiB, and coverage area and charges of overpotential from KOH to TMAOH. (c) Raman spectra of MEB and CoFeNiB, measured after running at 1.55 V in TMAOH. (d) PDOS of surface Co, Fe, Ni, Mn and O atoms in the CoFeNiMnOOH model, where the results of CoFeNiOOH are presented as gray lines. (e) Schematic band diagrams of CoFeNiOOH and CoFeNiMnOOH. (f) Calculated free energies of OER steps on CoFeNiMnOOH and CoFeNiOOH. (g) The adsorption energy for *Cl. (h) Corrosion resistance mechanism diagram.

First-principles density functional theory (DFT) simulations were systematically conducted to elucidate the fundamental OER mechanism on MEB catalysts. OER catalysts typically undergo in situ reconstruction into (oxy)hydroxides on the NF surface, where M-OOH species serve as the true active sites (Fig. S41). To assess the reactivity of lattice oxygen, we analyzed the density of states (DOS) for the O 2p and metal 3d orbitals. Comparative examination of orbital-projected DOS demonstrates that the O 2p-band center in Mn-incorporated CoFeNiOOH (−3.87 eV) exhibits a significant upshift toward Fermi level (E_F) compared to the undoped counterpart (−4.12 eV) (Fig. 5d). This electronic structure modification confirms that Mn introduction facilitates lattice oxygen participation in the catalytic cycle through the LOM. From the perspective of molecular orbital theory, intense d-electron correlations induce significant Mott-Hubbard band splitting, generating distinct electronic states: an unoccupied upper Hubbard band (UHB) and an occupied lower Hubbard band (LHB). The magnitude of their energy separation (ΔU) serves as a crucial descriptor for oxygen redox activity, with enhanced LOM propensity observed at larger ΔU values. We compared the ΔU values for CoFeNiMnOOH ($\Delta U_1 = -5.39$ eV) and CoFeNiOOH ($\Delta U_2 = -5.10$ eV) (Fig. 5e and Table S8). These results show that Mn doping lowers the metal LHB, increases ΔU, and weakens metal-oxygen bonds. To further investigate the OER stability of CoFeNiMnOOH and clarify the role of Mn incorporation, we performed formation energy calculations [63,64]. The results, consistent with the long-term stability tests, show that Mn incorporation substantially lowers the formation energy of CoFeNiOOH ($\Delta E = -7.86$ eV, Fig. S42), thereby enhancing its intrinsic structural stability.

A comparative analysis of the AEM and LOM pathways was conducted for both CoFeNiMnOOH and CoFeNiOOH, including Gibbs free energy calculations of adsorption intermediates. As shown in Fig. 5f, CoFeNiOOH exhibits deprotonation as the RDS in the AEM pathway, whereas O-O bond formation becomes the RDS in CoFeNiMnOOH. For the LOM pathway, the RDS in both catalysts involves the release of lattice oxygen, leading to the formation of surface oxygen vacancies. Notably, the RDS energy barrier for CoFeNiOOH is 0.71 eV in the AEM pathway but 1.44 eV in the LOM pathway, confirming its preferential AEM activity. In contrast, CoFeNiMnOOH displays a lower LOM barrier (0.59 eV) than AEM (0.63 eV), suggesting dominant LOM behavior. Moreover, the LOM RDS barrier of CoFeNiMnOOH is lower than the AEM RDS barrier of CoFeNiOOH, indicating faster overall kinetics for CoFeNiMnOOH (Fig. S43-44 and Table S9). Collectively, these findings confirm that Mn incorporation promotes the LOM pathway and accelerates catalyst reconstruction. In addition, to elucidate the protective role of Mn under corrosive conditions, we systematically evaluated the Cl- adsorption energies at different metal sites (Co, Fe, and Ni). DFT results reveal that Mn incorporation significantly strengthens the Cl^- repulsion effect, with Co sites showing the strongest repulsion ($E_{ads} = -1.706$ eV), while Fe and Ni sites exhibit weaker repulsion ($E_{ads} = -1.968$ and -1.801 eV, respectively). This suppression of Cl^- adsorption effectively protects both the catalyst and the NF substrate from corrosion (Fig. 5g, S45, and Table S10). These findings highlight that high-entropy effects induced by Mn incorporation play a crucial role in enhancing corrosion resistance and long-term durability in alkaline seawater environments. These findings highlight how strategic Mn incorporation significantly improves the catalyst's tolerance to chloride-containing environments.

4. Conclusions

In summary, we synthesized uniform nanofilm oxygen electrocatalysts via an innovative photo-assisted electrodeposition method to address the challenges of low activity and instability in seawater electrolysis. The MEB exhibited low overpotentials (350 mV@400 mA cm^{-2} in alkaline solution; 420 mV@400 mA cm^{-2} in alkaline seawater solution), excellent stability (4000 h@100 mA cm^{-2}), and high selectivity. CoFeNiMnOOH activates the LOM, thereby lowering the energy barrier for oxygen-containing intermediates. Meanwhile, configurational entropy-tailored borides enhance OH^- adsorption and accelerate the surface reconstruction process. Additionally, the surface OH^- species repel Cl^- ions via electrostatic interactions, improving OER selectivity during seawater electrolysis. The catalyst also delivered outstanding performance in an AEM system, achieving 1 A cm^{-2}. These findings provide valuable insights for designing highly efficient and corrosion-resistant non-precious-metal electrocatalysts.

CRediT authorship contribution statement

Baigang An: Writing – review & editing, Validation, Methodology. **Lixiang Li:** Formal analysis. **Chengguo Sun:** Formal analysis, Data curation. **Shuai Chen:** Writing – original draft, Investigation, Formal analysis, Data curation. **Han Zhang:** Project administration, Funding acquisition, Data curation. **Lin Wu:** Writing – review & editing, Data curation. **Shuo Zheng:** Formal analysis. **Yongjia Li:** Writing – review & editing, Supervision.

Declaration of Competing Interest

There are no conflicts to declare.

Acknowledgements

The authors gratefully acknowledge financial supported by the National Natural Science Foundation of China (22109061, 11972178 and 51972156), the Nature Science Foundation of Liaoning Province (2022-BS-283), and Technology Liaoning Project Grants (601010326). Key Project supported by the Research Foundation of Education Bureau of Liaoning Province (No. JYTZD2023093), Distinguished Professor Project of Education Department of Liaoning and the Open Project Found of Key Laboratory of Energy Materials and Electrochemistry Liaoning Province are acknowledged.

Appendix A. Supporting information

Supplementary data associated with this article can be found in the online version at doi:10.1016/j.nanoen.2025.111454.

Data availability

Data will be made available on request.

References

[1] S. Zhao, Y. Yang, Z. Tang, Insight into structural evolution, active sites, and stability of heterogeneous electrocatalysts, Angew. Chem. Int. Ed. 61 (2022) e202110186, https://doi.org/10.1002/anie.202110186.

[2] A. Zhu, L. Qiao, K. Liu, G. Gan, C. Luan, D. Lin, Y. Zhou, S. Bu, T. Zhang, K. Liu, T. Song, H. Liu, H. Li, G. Hong, W. Zhang, Rational design of precatalysts and controlled evolution of catalyst-electrolyte interface for efficient hydrogen production, Nat. Commun. 16 (2025) 1880, https://doi.org/10.1038/s41467-025-57056-6.

[3] R. Liu, Z. Gong, J. Liu, J. Dong, J. Liao, H. Liu, H. Huang, J. Liu, M. Yan, K. Huang, H. Gong, J. Zhu, C. Cui, G. Ye, H. Fei, Design of aligned porous carbon films with single-atom Co-N-C sites for high-current-density hydrogen generation, Adv. Mater. 33 (2021) e2103533, https://doi.org/10.1002/adma.202103533.

[4] H. Liu, Z. Zhang, J. Fang, M. Li, M.G. Sendeku, X. Wang, H. Wu, Y. Li, J. Ge, Z. Zhuang, D. Zhou, Y. Kuang, X. Sun, Eliminating over-oxidation of ruthenium oxides by niobium for highly stable electrocatalytic oxygen evolution in acidic media, Joule 7 (2023) 558–573, https://doi.org/10.1016/j.joule.2023.02.012.

[5] Y. Wang, M. Wang, Y. Yang, D. Kong, C. Meng, D. Zhang, H. Hu, M. Wu, Potential technology for seawater electrolysis: Anion-exchange membrane water electrolysis, Chem. Catal. 3 (2023) 100643, https://doi.org/10.1016/j.checat.2023.100643.

[6] T. Wang, Y. Yuan, W. Shi, G. Li, P. Rao, J. Li, Z. Kang, X. Tian, Hydrogen production from seawater electrolysis, Chem. Commun. 61 (2025) 1719–1728, https://doi.org/10.1039/d4cc05143b.

[7] M. Ning, F. Zhang, L. Wu, X. Xing, D. Wang, S. Song, Q. Zhou, L. Yu, J. Bao, S. Chen, Z. Ren, Boosting efficient alkaline fresh water and seawater electrolysis via electrochemical reconstruction, Energy Environ. Sci. 15 (2022) 3945–3957, https://doi.org/10.1039/d2ee01094a.

[8] X. Zhang, Z. Zuo, C. Liao, F. Jia, C. Cheng, Z. Guo, Strategies for designing advanced transition metal-based electrocatalysts for alkaline water/seawater splitting at ampere-level current densities, ACS Catal. 14 (2024) 18055–18071, https://doi.org/10.1021/acscatal.4c06509.

[9] T. Ma, W. Xu, B. Li, X. Chen, J. Zhao, S. Wan, K. Jiang, S. Zhang, Z. Wang, Z. Tian, Z. Lu, L. Chen, The critical role of additive sulfate for stable alkaline seawater oxidation on nickel-based electrodes, Angew. Chem. Int. Ed. 133 (2021) 22922–22926, https://doi.org/10.1002/ange.202110355.

[10] P.-J. Deng, R. Xue, J. Lu, P. Tsiakaras, Strategies for designing anti-chlorine corrosion catalysts in seawater splitting, Adv. Energy Mater. 15 (2025) 2405749, https://doi.org/10.1002/aenm.202405749.

[11] L. Sharma, N.K. Katiyar, A. Parui, R. Das, R. Kumar, C.S. Tiwary, A.K. Singh, A. Halder, K. Biswas, Low-cost high entropy alloy (HEA) for high-efficiency oxygen evolution reaction (OER), Nano Res. 15 (2022) 4799–4806, https://doi.org/10.1007/s12274-021-3802-4.

[12] X. Wang, Q. Peng, X. Zhang, X. Lv, X. Wang, Y. Fu, Carbonaceous-assisted confinement synthesis of refractory high-entropy alloy nanocomposites and their application for seawater electrolysis, J. Colloid Interf. Sci. 607 (2022) 1580–1588, https://doi.org/10.1016/j.jcis.2021.08.201.

[13] P. Li, Y. Yao, W. Ouyang, Z. Liu, H. Yin, D. Wang, A stable oxygen evolution splitting electrocatalysts high entropy alloy FeCoNiMnMo in simulated seawater, J. Mater. Sci. Technol. 138 (2023) 29–35, https://doi.org/10.1016/j.jmst.2022.08.012.

[14] J. Wang, P. Jiang, F. Yuan, X. Wu, Chemical medium-range order in a medium-entropy alloy, Nat. Commun. 13 (2022) 1021, https://doi.org/10.1038/s41467-022-28687-w.

[15] H. Wu, J. Zhang, Q. Lu, Y. Li, R. Jiang, Y. Liu, X. Zheng, N. Zhao, J. Li, Y. Deng, W. Hu, High-entropy layered double hydroxides with highly adjustable components for enhancing electrocatalytic oxygen evolution, ACS Appl. Mater. Interfaces 15 (2023) 38423–38432, https://doi.org/10.1021/acsami.3c05781.

[16] L. Liu, T. Liu, C. Xu, W. Zhao, J. Fan, J. Liu, X. Ma, W. Fu, FeCoCuMnRuB nanobox with dual driving of high-entropy and electron-trap effects as the efficient electrocatalyst for water oxidation, Nano Lett. 24 (2024) 2831–2838, https://doi.org/10.1021/acs.nanolett.3c04962.

[17] D. Li, C. Liu, S. Tao, J. Cai, B. Zhong, J. Li, W. Deng, H. Hou, G. Zou, X. Ji, High-entropy electrode materials: synthesis, properties and outlook, Nano-micro Lett. 17 (2024) 22, https://doi.org/10.1007/s40820-024-01504-3.

[18] A. Hai, M. Daud, G. Mujtaba, F. Banat, M.A. Al-Harthi, A comprehensive review of two-dimensional high-entropy layered hydroxides: synthesis, characterization, and applications, Coord. Chem. Rev. 529 (2025) 216435, https://doi.org/10.1016/j.ccr. 2025.216435.

[19] X. Han, Q. Chen, Q. Chen, Q. Wu, Z. Xu, T. Zheng, W. Li, D. Cui, Z. Duan, J. Zhang, J. Li, H. Li, Z. Wang, J. Wang, Z. Xia, Eutectic dual-phase microstructure modulated porous high-entropy alloys as high-performance bifunctional electrocatalysts for water splitting, J. Mater. Chem. A 10 (2022) 11110–11120, https://doi.org/10.1039/d2ta01701f.

[20] H. Liu, H. Qin, J. Kang, L. Ma, G. Chen, Q. Huang, Z. Zhang, E. Liu, H. Lu, J. Li, N. Zhao, A freestanding nanoporous NiCoFeMoMn high-entropy alloy as an efficient electrocatalyst for rapid water splitting, Chem. Eng. J. 435 (2022) 134898, https://doi.org/10.1016/j.cej.2022.134898.

[21] W.-J. Liu, Y.-H. Chang, Y.-T. Chen, Y.-C. Chiang, Y.-C. Liu, T.-H. Wu, P.-W. Chi, Effect of annealing on the structural, magnetic and surface energy of CoFeBY films on Si (100) substrate, Materials 14 (2021) 987, https://doi.org/10.3390/ma14040987.

[22] C.C. Zhang, X. Gao, B. Yilmaz, Development of FTIR spectroscopy methodology for characterization of boron species in FCC catalysts, Catalysts 10 (2020) 1327, https://doi.org/10.3390/catal10111327.

[23] L. Li, S. Ma, X. Liu, Y. Yue, J. Hui, R. Xu, Y. Bao, J. Rocha, Synthesis and characterization of tetraborate pillared hydrotalcite, Chem. Mater. 8 (1996) 204–208, https://doi.org/10.1021/cm950319w.

[24] H. Yang, Z. Chen, P. Guo, B. Fei, R. Wu, B-doping-induced amorphization of LDH for large-current-density hydrogen evolution reaction, Appl. Catal. B 261 (2020) 118240, https://doi.org/10.1016/j.apcatb.2019.118240.

[25] M. Zhang, K. Luo, Y. Fan, X. Lu, J. Ye, N. Lu, J. Dong, Q. Niu, J. Zhang, P. Zhang, S. Dai, Metal vacancies and self-reconstruction of high entropy metal borates to boost the oxygen evolution reaction, Chem. Eng. J. 493 (2024) 152758, https://doi.org/10.1016/j.cej.2024.152758.

[26] Y. Wang, S. Tao, H. Lin, G. Wang, K. Zhao, R. Cai, K. Tao, C. Zhang, M. Sun, J. Hu, B. Huang, S. Yang, Atomically targeting NiFe LDH to create multivacancies for OER catalysis with a small organic anchor, Nano Energy 81 (2021) 105606, https://doi.org/10.1016/j.nanoen.2020.105606.

[27] W. Ma, Y. Zhang, B. Wang, J. Wang, Y. Dai, L. Hu, X. Lv, J. Dang, Significantly enhanced OER and HER performance of NiCo-LDH and NiCoP under industrial water splitting conditions through ru and mn bimetallic co-doping strategy, Chem. Eng. J. 494 (2024) 153212, https://doi.org/10.1016/j.cej.2024.153212.

[28] W. Fu, J. Li, Y. Liu, S. Yao, S. Wang, K. Ji, X. Wang, L. Shi, X. Li, F. Zhang, J. Xie, Z. Yang, Y.-M. Yan, Asymmetric oxygen vacancies in cu - ov - mn units boost charge transfer in MnO_2 for enhanced hybrid capacitive deionization efficiency, Desalination 613 (2025) 119000, https://doi.org/10.1016/j.desal.2025.119000.

[29] D. Zhou, Z. Cai, Y. Jia, X. Xiong, Q. Xie, S. Wang, Y. Zhang, W. Liu, H. Duan, X. Sun, Activating basal plane in NiFe layered double hydroxide by Mn^{2+} doping for efficient and durable oxygen evolution reaction, Nanoscale Horiz. 3 (2018) 532–537, https://doi.org/10.1039/c8nh00121a.

[30] L. Yan, Y. Ren, X. Zhang, Y. Sun, J. Ning, Y. Zhong, B. Teng, Y. Hu, Electronic modulation of composite electrocatalysts derived from layered NiFeMn triple hydroxide nanosheets for boosted overall water splitting, Nanoscale 11 (2019) 20797–20808, https://doi.org/10.1039/c9nr07159h.

[31] M. Moloudi, A. Noori, M.S. Rahmanifar, Y. Shabangoli, M.F. El-Kady, N. B. Mohamed, R.B. Kaner, M.F. Mousavi, Layered double hydroxide templated synthesis of amorphous NiCoFeB as a multifunctional electrocatalyst for overall water splitting and rechargeable zinc-air batteries, Adv. Energy Mater. 13 (2023) 2203002, https://doi.org/10.1002/aenm.202203002.

[32] P. Zhai, C. Wang, Y. Zhao, Y. Zhang, J. Gao, L. Sun, J. Hou, Regulating electronic states of nitride/hydroxide to accelerate kinetics for oxygen evolution at large current density, Nat. Commun. 14 (2023) 1873, https://doi.org/10.1038/s41467-023-37091-x.

[33] D.K. Bediako, Y. Surendranath, D.G. Nocera, Mechanistic studies of the oxygen evolution reaction mediated by a nickel-borate thin film electrocatalyst, J. Am. Chem. Soc. 135 (2013) 3662–3674, https://doi.org/10.1021/ja3126432.

[34] A. Alobaid, C. Wang, R.A. Adomaitis, Mechanism and kinetics of HER and OER on NiFe LDH films in an alkaline electrolyte, J. Electrochem. Soc. 165 (2018) J3395–J3404, https://doi.org/10.1149/2.0481815jes.

[35] Z. Liang, D. Shen, Y. Wei, F. Sun, Y. Xie, L. Wang, H. Fu, Modulating the electronic structure of cobalt-vanadium bimetal catalysts for high-stable anion exchange membrane water electrolyzer, Adv. Mater. 36 (2024) e2408634, https://doi.org/10.1002/adma.202408634.

[36] Y.-F. Chen, J.-H. Li, T.-T. Liu, S.-H. You, P. Liu, F.-J. Li, M.-Q. Gao, S.-G. Chen, F.-F. Zhang, Constructing robust NiFe LDHs–NiFe alloy gradient hybrid bifunctional catalyst for overall water splitting: one-step electrodeposition and surface reconstruction, Rare Metals. 42 (2023) 2272–2283, https://doi.org/10.1007/s12598-022-02249-x.

[37] J. Kibsgaard, T.F. Jaramillo, Molybdenum phosphosulfide: an active, acid-stable, earth-abundant catalyst for the hydrogen evolution reaction, Angew. Chem. Int. Ed. 53 (2014) 14433–14437, https://doi.org/10.1002/anie.201408222.

[38] S. Anantharaj, S. Kundu, Do the evaluation parameters reflect intrinsic activity of electrocatalysts in electrochemical water splitting? ACS Energy Lett. 4 (2019) 1260–1264, https://doi.org/10.1021/acsenergylett.9b00686.

[39] J. Sun, S. Zhou, Z. Zhao, S. Qin, X. Meng, C.-H. Tung, L.-Z. Wu, Deep reconstruction of a Mo-based electrocatalyst for high-performance water/seawater oxidation at ampere-level current density, Energy Environ. Sci. 18 (2025) 1952–1962, https://doi.org/10.1039/d4ee04941a.

[40] H. Lei, L. Ma, Q. Wan, S. Tan, B. Yang, Z. Wang, W. Mai, H.J. Fan, Promoting surface reconstruction of NiFe layered double hydroxide for enhanced oxygen evolution, Adv. Energy Mater. 12 (2022) 2202522, https://doi.org/10.1002/aenm.202202522.

[41] W. Liu, J. Yu, T. Li, S. Li, B. Ding, X. Guo, A. Cao, Q. Sha, D. Zhou, Y. Kuang, X. Sun, Self-protecting CoFeAl-layered double hydroxides enable stable and efficient brine oxidation at 2 A cm^{-2}, Nat. Commun. 15 (2024) 4712, https://doi.org/10.1038/s41467-024-49195-z.

[42] J.-H. Li, H. Chen, S.-H. You, G.-X. Yang, P. Liu, M.-Q. Gao, S.-G. Chen, F.-F. Zhang, Highly anti-corrosive NiFe LDHs–NiFe alloy hybrid enables long-term stable alkaline seawater electrolysis, Rare Metals. 43 (2024) 4321–4332, https://doi.org/10.1007/s12598-024-02780-z.

[43] L. Shao, X. Han, L. Shi, T. Wang, Y. Zhang, Z. Jiang, Z. Yin, X. Zheng, J. Li, X. Han, Y. Deng, In situ generation of molybdate-modulated nickel-iron oxide electrodes with high corrosion resistance for efficient seawater electrolysis, Adv. Energy Mater. (2023), https://doi.org/10.1002/aenm.202303261.

[44] C. Feng, Y. Zhou, Z. Xie, Z. Yang, L. Zou, P. Wang, W. Lian, P. Xiaokaiti, Y. Kansha, A. Abudula, G. Guan, Vanadium boosted high-entropy amorphous FeCoNiMoV oxide for ampere-level seawater oxidation, Chem. Eng. J. 495 (2024) 153408 https:// doi.org/10.1016/j.cej.2024.153408.

[45] C. Huang, Q. Zhou, D. Duan, L. Yu, W. Zhang, Z. Wang, J. Liu, B. Peng, P. An, J. Zhang, L. Li, J. Yu, Y. Yu, The rapid self-reconstruction of Fe-modified Ni hydroxysulfide for efficient and stable large-current-density water/seawater oxidation, Energy Environ. Sci. 15 (2022) 4647–4658, https://doi.org/10.1039/d2ee01478e.

[46] R.-T. Gao, Z. Gao, N.T. Nguyen, J. Chen, X. Liu, L. Wang, L. Wu, Photoelectrochemical production of disinfectants from seawater, Nat. Sustain. (2025), https://doi.org/10.1038/s41893-025-01530-y.

[47] H. Guan, Y. Liu, X. Hu, J. Wu, T.-N. Ye, Y. Lu, H. Hosono, Q. Li, F. Pan, Dipole coupling accelerated H_2O dissociation by magnesium-based intermetallic catalysts, Angew. Chem. Int. Ed. 63 (2024) e202400119, https://doi.org/10.1002/anie.202400119.

[48] W. Liao, F. Qing, Q. Liu, R. Wu, C. Zhou, L. Chen, Y. Chen, X. Li, Carbothermal shock synthesis of lattice oxygen-mediated high-entropy FeCoNiCuMo-O electrocatalyst with a fast kinetic, high efficiency, and stable oxygen evolution reaction, Nano Lett. 25 (2025) 1575–1583, https://doi.org/10.1021/acs.nanolett.4c05658.

[49] D. Zhou, S. Wang, Y. Jia, X. Xiong, H. Yang, S. Liu, J. Tang, J. Zhang, D. Liu, L. Zheng, Y. Kuang, X. Sun, B. Liu, NiFe hydroxide lattice tensile strain: enhancement of adsorption of oxygenated intermediates for efficient water oxidation catalysis, Angew. Chem. Int. Ed. 58 (2019) 736–740, https://doi.org/10.1002/anie.201809689.

[50] G. Quanxin, L. Yu, X. Zhengrong, L. Rui, CeO_2-Accelerated surface reconstruction of $CoSe_2$ nanoneedle forms active CeO_2@CoOOH interface to boost oxygen evolution reaction for water splitting, Adv. Energy Mater. (2024), https://doi.org/10.1002/aenm.202403744.

[51] H.-Y. Wang, S.-F. Hung, H.-Y. Chen, T.-S. Chan, H.M. Chen, B. Liu, In operando identification of geometrical-site-dependent water oxidation activity of spinel Co_3O_4, J. Am. Chem. Soc. 138 (2016) 36–39, https://doi.org/10.1021/jacs.5b10525.

[52] Z. Xiao, Y.-C. Huang, C.-L. Dong, C. Xie, Z. Liu, S. Du, W. Chen, D. Yan, L. Tao, Z. Shu, G. Zhang, H. Duan, Y. Wang, Y. Zou, R. Chen, S. Wang, Operando identification of the dynamic behavior of oxygen vacancy-rich Co_3O_4 for oxygen evolution reaction, J. Am. Chem. Soc. 142 (2020) 12087–12095, https://doi.org/10.1021/jacs.0c00257.

[53] Z. Lu, L. Qian, Y. Tian, Y. Li, X. Sun, X. Duan, Ternary NiFeMn layered double hydroxides as highly-efficient oxygen evolution catalysts, Chem. Commun. 52 (2016) 908–911, https://doi.org/10.1039/c5cc08845c.

[54] Y.-J. Wu, J. Yang, T.-X. Tu, W.-Q. Li, P.-F. Zhang, Y. Zhou, J.-F. Li, J.-T. Li, S.-G. Sun, Evolution of cationic vacancy defects: a motif for surface restructuration of OER precatalyst, Angew. Chem. Int. Ed. 60 (2021) 26829–26836, https://doi.org/10.1002/anie.202112447.

[55] T. Li, Z. Wang, L. Wang, M. Wang, Y.-Q. Liu, Nd and Ni Co-doped spinel Co_3O_4 nanosheet as an effective electrocatalyst for oxygen evolution reaction, Appl. Catal. B 352 (2024) 123990, https://doi.org/10.1016/j.apcatb.2024.123990.

[56] Z.-X. Qian, G.-H. Liang, L.-F. Shen, G. Zhang, S. Zheng, J.-H. Tian, J.-F. Li, H. Zhang, Phase engineering facilitates O-O coupling via lattice oxygen mechanism for enhanced oxygen evolution on nickel-iron phosphide, J. Am. Chem. Soc. 147 (2025) 1334–1343, https://doi.org/10.1021/jacs.4c15847.

[57] J. Wang, Y. Liu, G. Yang, Y. Jiao, Y. Dong, C. Tian, H. Yan, H. Fu, MXene-Assisted NiFe sulfides for high-performance anion exchange membrane seawater electrolysis, Nat. Commun. 16 (2025) 1319, https://doi.org/10.1038/s41467-025-56639-7.

[58] Q. Jiang, S. Wang, C. Zhang, Z. Sheng, H. Zhang, R. Feng, Y. Ni, X. Tang, Y. Gu, X. Zhou, S. Lee, D. Zhang, F. Song, Active oxygen species mediate the iron-promoting electrocatalysis of oxygen evolution reaction on metal oxyhydroxides, Nat. Commun. 14 (2023) 6826, https://doi.org/10.1038/s41467-023-42646-z.

[59] X. Luo, H. Zhao, X. Tan, S. Lin, K. Yu, X. Mu, Z. Tao, P. Ji, S. Mu, Fe-S dually modulated adsorbate evolution and lattice oxygen compatible mechanism for water oxidation, Nat. Commun. 15 (2024) 8293, https://doi.org/10.1038/s41467-024-52682-y.

[60] L. Liu, J. Cao, S. Hu, T. Liu, C. Xu, W. Fu, X. Ma, X. Yang, Antagonism effect of residual s triggers the dual-path mechanism for water oxidation, J. Energy Chem. 93 (2024) 568–579, https://doi.org/10.1016/j.jechem.2024.02.028.

[61] Y. Li, J. Liu, S. Li, S. Peng, Codecoration of phosphate and iron for improving oxygen evolution reaction of layered $Ni(OH)_2$/NiOOH, ACS Catal. (2024) 4807–4819, https://doi.org/10.1021/acscatal.4c00229.

[62] Z.-F. Huang, S. Xi, J. Song, S. Dou, X. Li, Y. Du, C. Diao, Z.J. Xu, X. Wang, Tuning of lattice oxygen reactivity and scaling relation to construct better oxygen evolution electrocatalyst, Nat. Commun. 12 (2021) 3992, https://doi.org/10.1038/s41467-021-24182-w.

[63] Y. Zou, J.M. Wheeler, H. Ma, P. Okle, R. Spolenak, Nanocrystalline high-entropy alloys: a new paradigm in high-temperature strength and stability, Nano Lett. 17 (2017) 1569–1574, https://doi.org/10.1021/acs.nanolett.6b04716.

[64] K. Zhang, G. Zhang, J. Qu, H. Liu, Disordering the atomic structure of co(II) oxide via B-doping: an efficient oxygen vacancy introduction approach for high oxygen evolution reaction electrocatalysts, Small 14 (2018) e1802760, https://doi.org/10.1002/smll.201802760.

Shuai Chen is currently a postgraduate student at University of Science and Technology Liaoning, China. His current research focuses on non-precious metal materials, electrolysis of seawater for hydrogen production, as well as the design and structural optimization of electrode.

Han Zhang is associate professor of University of Science and Technology Liaoning, China. He received his Ph.D Dalian University of Technology in 2019 supervised by Prof. Zongbin Zhao. His research interests primarily focus on the rational design and optimization of carbon-based nanohybrids for energy storage and conversion applications.

Lin Wu is currently a Ph.D at University of Science and Technology Liaoning, China. She obtained his B.S. degree from University of Science and Technology Liaoning in 2020.

Shuo Zheng is currently a postgraduate student at University of Science and Technology Liaoning, China.

Yongjia Li is currently a postgraduate student at University of Science and Technology Liaoning, China.

Lixiang Li is a professor of University of Science and Technology Liaoning, China. She received her Ph.D in material science at Institute of Metal Research, Chinese Academy of Sciences in 2005 supervised by Prof. Hui-Ming Cheng. She had ever worked as a postdoctoral fellow at Tohoku University and a visiting scholar at the University of Michigan (Ann Arbor).

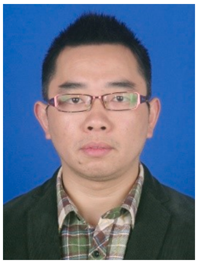

Chengguo Sun received his Ph.D degree in chemical engineering and technology at Nanjing University of Science and Technology, China in 2014. He was working as a postdoctoral researcher, cooperated with Prof. Feng Li as supervisor, at institute of Metal Research, Chinese Academy of Science. He currently working as a full professor at Nanjing University of Science and Technology and a part-time professor at University of Science and Technology Liaoning.

Baigang An is a professor of University of Science and Technology Liaoning, China. He received his Ph.D in Applied Chemistry at Tianjin University in 2003 supervised by Prof. Shi-zhe Song. He had ever worked as a research fellow at Tohoku University and a visiting scholar at the University of Michigan (Ann Arbor).